Effect of the deposition temperature on the electrochemical properties of $La_{0.6}Sr_{0.4}Co_{0.8}Fe_{0.2}O_{3-\delta}$ cathode prepared by conventional spray-pyrolysis

CrossMark

D. Marrero-López*, R. Romero, F. Martín, J.R. Ramos-Barrado

Lab. de Materiales y Superficies, Dpto. de Física Aplicada I e Ingeniería Química, Universidad de Málaga, 29071 Málaga, Spain

HIGHLIGHTS

- LSCF film cathodes prepared by conventional spray pyrolysis on CGO electrolytes.
- Porous, cracked and macroporous electrodes were obtained between 250 and 450 °C.
- All cells annealed at 650 °C showed ASR values as low as 0.04 Ω cm² at 650 °C.
- Porous electrodes exhibited lower performance degradation with the thermal treatment.

GRAPHICAL ABSTRACT
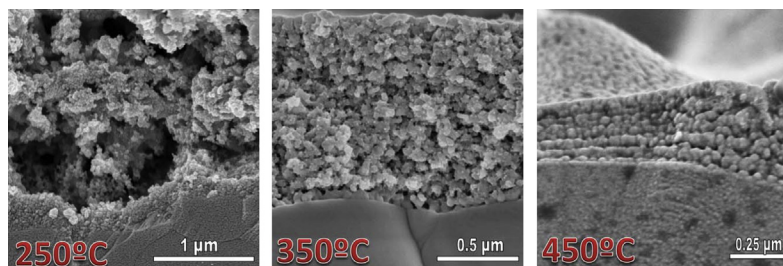
ARTICLE INFO

ABSTRACT

$La_{0.6}Sr_{0.4}Co_{0.8}Fe_{0.2}O_{3-\delta}$ (LSCF) cathodes have been deposited by conventional spray pyrolysis on $Ce_{0.8}Gd_{0.2}O_{1.9}$ (CGO) electrolytes at different temperatures between 250 and 450 °C, obtaining electrodes with different microstructure and porosity. Highly porous and macroporous electrodes are obtained at deposition temperatures of 250 °C and 450 °C, respectively, with an average grain size of 30–50 nm. The influence of the post-annealing treatment on the microstructure and on the electrochemical properties is investigated by scanning electron microscopy and impedance spectroscopy in air and as a function of the oxygen partial pressure to identify the different contributions to the polarization. Samples annealed at 650 °C show similar values of area specific resistance 0.04–0.06 Ω cm² at a measured temperature of 650 °C. However, after annealing the samples at 850 °C, the ASR values increase up to 0.1–0.6 Ω cm² with the lowest value corresponding to the film deposited at 250 °C due to the large porosity and surface area of this film. The performance degradation upon annealing is attributed to decreasing reaction sites induced by grain growth and densification.

© 2014 Elsevier B.V. All rights reserved.

1. Introduction

One of the major targets for the development of solid oxide fuel cell (SOFCs) is the reduction of the operating temperatures below 700 °C [1,2]. This would have several benefits, such as reduction of operation costs, shorten start-up time and cell durability. The performance of a SOFC at low temperatures depends on the ohmic resistance of the electrolyte, although it can be lowered by reducing the electrolyte thickness. Another important limiting factor is the increase of the cathode polarization due to the thermally activated nature of the oxygen reduction reaction (ORR), involving multiple mechanistic steps from oxygen adsorption to incorporation into the electrolyte lattice at electrochemically active triple phase boundaries (TPB) [3–5].

* Corresponding author. Present address: Dpto. de Física Aplicada I, Laboratorio de Materiales y Superficies (Unidad Asociada al C.S.I.C.), Facultad de Ciencias, Campus de Teatinos, Universidad de Málaga, 29071 Málaga, Spain. Tel.: +34 952137057; fax: +34 952132382.

E-mail addresses: damarre@uma.es, marrero@uma.es (D. Marrero-López).

The state-of-the-art cathode material, $La_{0.8}Sr_{0.2}MnO_{3-\delta}$ (LSM), exhibits negligible ionic conductivity and a high activation energy for ORR at low temperature <800 °C, leading to a significant reduction of the electrochemical performance. To overcome this limitation, different mixed ionic-electronic conductors (MIEC), such as $La_{1-x}Sr_xCo_{1-y}Fe_yO_{3-\delta}$ (LSCF), $Ba_{0.5}Sr_{0.5}Co_{0.8}Fe_{0.2}O_{3-\delta}$ (BSCF) and $GdBaCo_2O_{5+\delta}$, have been investigated as alternative cathodes to LSM, possessing better performance in the intermediate temperature range 500–800 °C [6–8]. LSCF are between the most studied cathodes for applications at low temperature due to the better phase stability compared to other cathode materials, such as BSCF which shows degradation due to phase segregation and carbonation [9].

The efficiency of these cathodes is related to the intrinsic electrochemical properties but also the fabrication process is important to produce electrode microstructures with high surface area and porosity that facilitate the diffusion of the oxygen gas to the active sites, leading to lower polarization resistances [10–12].

Precursor routes have been used to obtain nanocrystalline powders of different cathode materials with high surface area and better electrochemical properties, however, the subsequent electrode deposition steps at elevate temperatures, such as tape-casting or screen-printing, produce an excessive grain growth and a reduction of the porosity, resulting consequently in a decrease of the performance. For this reason, alternative deposition methods in a simple one step at low temperatures are required to produce electrode morphologies with high surface areas and large number of active sites for ORR. In this context, thin films cathodes deposited at reduced temperatures by different physical and wet chemical methods have showed enhanced performance [13]. For instance, electrostatic spray deposition was used to obtain LSM and LSM/YSZ composite [14,15], $Sm_{0.5}Sr_{0.5}O_{3-\delta}$ [16,17] and $La_{1-x}Sr_xCo_{1-y}Sr_yO_{3-\delta}$ cathodes [18–23].

In this work, a simple, low-cost, and environmentally friendly method based on spray-pyrolysis was used to prepare $La_{0.6}Sr_{0.4}Co_{0.8}Fe_{0.2}O_{3-\delta}$ (LSCF) cathodes on $Ce_{0.9}Gd_{0.1}O_{1.95}$ (CGO) electrolyte by using aqueous precursor solutions. By varying the deposition temperature, LSCF films with different morphology and porosity were obtained. The polarization resistance of different LSCF symmetrical cells was evaluated using electrochemical impedance spectroscopy in air and as a function of the oxygen partial pressure. The influence of the post-deposition temperature on the electrode microstructure and on the polarization resistance was also investigated.

2. Experimental

2.1. Cathode deposition

Cathodes with composition $La_{0.6}Sr_{0.4}Co_{0.8}Fe_{0.2}O_{3-\delta}$ were deposited by using a homemade spray-pyrolysis apparatus at different deposition temperatures between 250 and 450 °C.

The precursor solutions were obtained by dissolving stoichiometric quantities of $La(NO_3)_3 \cdot 6H_2O$ (99.99%), $Sr(NO_3)_2$ (99.9%), $Co(NO_3)_2 \cdot 6H_2O$ (99%) and $Fe(NO_3)_3 \cdot 9H_2O$ (98%) in distilled water, all of them supplied from Sigma–Aldrich. The nitrates before weighting were analysed by thermogravimetric analysis to determine the correct water content. The concentration of the solution was 0.025 M of $La_{0.6}Sr_{0.4}Co_{0.8}Fe_{0.2}O_{3-\delta}$ in water. In this work, the use of organic-based solutions was avoided to prevent the formation of organic residues, which do not decompose up to very high temperatures.

The LSCF electrodes were deposited on quartz substrates for structural investigation and on $Ce_{0.8}Gd_{0.2}O_{1.9}$ (CGO) polycrystalline pellets for electrochemical characterization. The CGO pellets

(13 mm of diameter and 1 mm of thickness) were prepared from commercial powders (Praxair) by pressing them into pellets at 75 MPa and then sintered at 1400 °C for 4 h, reaching a relative density higher than 95%. CGO substrates were used as-sintered without polishing the pellet faces.

The precursor solution was sprayed onto the substrates, which are placed on a metal hot block at the desired temperature of pyrolysis, using resistance wires. A K-type thermocouple inserted in a hole drilled through the metal close to the substrate was used to monitor the block temperature. The substrate is moved underneath the spray nozzle, fixed in position, back and forth at a constant frequency, to obtain a more homogeneous deposition of the films [24].

The flow rate of the precursor solution was 20 ml h^{-1} using a syringe pump. A stream of compressed air gas through the nozzle, free of oil, is used for the atomization of the solution into very fine droplets. The air pressure was 2.5 bar, resulting in an air flux through the nozzle of approximately 20 l min^{-1} and the nozzle to substrate distance was 20 cm. The deposition time was fixed at 1 h. In this work the temperature was the only parameter modified for the different depositions, varying between 250 and 450 °C. After the deposition, the samples were annealed between 650 and 850 °C for 5 h in air to investigate the influence of the thermal treatment on the phase formation and on the microstructure evolution.

Similar symmetrical cells were also prepared using submicrometric LSCF powders obtained from citrate precursor method for comparison purpose, as reported elsewhere [25]. These powders were mixed in a 50 wt.% with Decoflux™ to obtain a slurry, which was screen-printed on both sides of the CGO pellets and then sintered at 900 °C for 1 h. The thickness of LSCF layer was approximately 40 μm.

2.2. Materials characterization

X-ray powder diffraction (XRD) patterns were obtained using a PANalytical X'Pert Pro diffractometer, equipped with a Ge(111) primary monochromator and the X'Celerator detector. The scans were collected in the 2θ range (20–80°) with 0.016° step for 1 h. The structural analysis and phase identification were done by using the FullProf and X'Pert HighScore Plus v.2.0e software [26,27].

The morphology of the electrodes was studied by scanning electron microscopy (JEOL SM-6490LV and a FEI Helios Nanolab 650). The average grain size of the films was estimated from the SEM micrographs by the linear intercept method with the help of Estereologia software [28].

The impedance spectra measurements were performed at open circuit voltage with a Solartron 1260 FRA in the 0.01–10^6 Hz frequency range and an amplitude voltage of 50 mV. Pt ink (Heraus) was applied onto the electrodes, to obtain a current collector layer, which was fired at 650 °C for 30 min to ensure good adherence and conductivity.

The symmetrical cells were firstly annealed at 650 °C and then at 750 and 850 °C for 5 h. The impedance spectra were acquired after each post-annealing treatment on the cooling process in steps of 50 °C with a dwell time of 30 min between consecutive measurements. The samples will be hereafter labelled as function of the deposition temperature and the subsequent post-annealing treatment, e.g. S250_650, where the first number, 250, indicates the deposition temperature and the second one, 650, the post-annealing treatment in air.

The impedance spectra were also collected as a function of the oxygen partial pressure (pO_2) from 1 to 10^{-2} atm with the help of an electrochemical cell, consisting of a YSZ tube closed at one end, with an electrochemical oxygen pump and sensor. The system was flushed with O_2 and N_2 gas mixture between 600 and 700 °C for 1 h

and the cells were equilibrated at each oxygen partial pressure at least for 30 min before acquiring the impedance spectra. The data were analysed with equivalent circuits using the ZView software [29].

3. Results

3.1. Phase formation and structure

Fig. 1a shows the XRD patterns of LSCF powders obtained by citrate method and films deposited on quartz substrate. According to the literature data LSCF has a phase transition from rhombohedral (s. g. $R\overline{3}c$) to cubic (s. g. $Pm\overline{3}m$), occurring at about 500 °C [30]. LSCF powders exhibit only the reflections associated with the cubic phase (s.g. $Pm\overline{3}m$) at 700 °C. However, after calcining the powders at 1000 °C, the typical splitting reflections of the rhombohedral phase (s. g. $R\overline{3}c$) are observed, as expected for this composition in agreement to the literature [31]. Thus, the stabilization of the cubic phase at room temperature for powders calcined at 700 °C is probably attributed to the small crystallite size (29 nm at 700 °C compared to ~110 nm at 1000 °C) due to the influence of the surface free energy and/or the oxygen non-stoichiometry. The same behaviour was observed in $La_{0.6}Sr_{0.4}CoO_{3-\delta}$ nanopowders [32].

The as-deposited films are amorphous and transform into the perovskite-type phase after calcination at 650 °C in air, without the presence of extra diffraction peaks associated with secondary phases. The crystallinity of the films is obviously improved with increasing temperature and the cubic phase seems to be retained in whole the temperature range studied between 650 and 850 °C with a crystallite size ranging from 24 nm at 650 °C to 35 nm at 850 °C.

The unit cell volume for powders prepared by citrate method decreases slightly with the sintering temperature from 56.745 Å³ at 700 °C to 56.620 Å³ at 1000 °C and a similar behaviour was observed in the films, i.e. 56.504 Å³ at 650 °C and 56.239 Å³ at 850 °C. The decrease of the cell volume with the annealing temperature can be explained by the ordering of the atoms in the lattice induced by crystallization. These values are in good agreement with those previously reported for similar compositions [31].

The XRD pattern of LSCF deposited on CGO pellets show two crystalline phases, corresponding to the perovskite LSCF and the fluorite CGO structures (Fig. 2). No secondary phases and no

significant peak shift are observed after annealing the films at 650–850 °C for 5 h, indicating that no reactivity took place between CGO and LSCF in the operating temperature range.

3.2. Microstructure

Fig. 2 shows the SEM image of the LSCF films after annealing at 650 °C for 5 h. The films show good adhesion to the substrates independently on the deposition temperature and no delamination in any of the CGO/LSCF interfaces was observed. The superficial morphology of the films changes significantly with the deposition temperature from rough porous at 250 °C (Fig. 3a) to dense and continuous at 450 °C (Fig. 3g). At intermediate temperatures (300–350 °C) porous and cracked films are obtained (Fig. 3d). These morphological changes are only attributed to the different deposition temperature, because the experimental parameters: solution concentration, flow rate, nozzle-substrate distance and deposition time were fixed for all preparations as detailed in the experimental section.

The LSCF films deposited at 250 °C have a very porous microstructure that extends throughout the whole thickness of the films ~3 μm, which ensures effective gas diffusion (Fig. 3a–c). The abundant solvent remaining after the deposition and eliminated in the subsequent post-annealing treatment produces a highly porous material without the formation of visible superficial cracks.

Porous and cracked films are obtained at 350 °C (Fig. 3d–f). These films have lower porosity and cracks are formed as consequence of the shrinkage and sintering of the film during the annealing treatment. It is important to note that the surface of the films densifies by annealing, resulting in a gradual decrease of the porosity over the film thickness. Similar observations were reported in the literature for LSCF thin films prepared by flame spray deposition [19].

At higher temperature, 450 °C, the arriving drops contain less solvent and thinner films ~0.25 μm with smaller porosity are obtained (Fig. 3i). Therefore, during the post-thermal treatment, a small volume change occurs, leading to crack-free films.
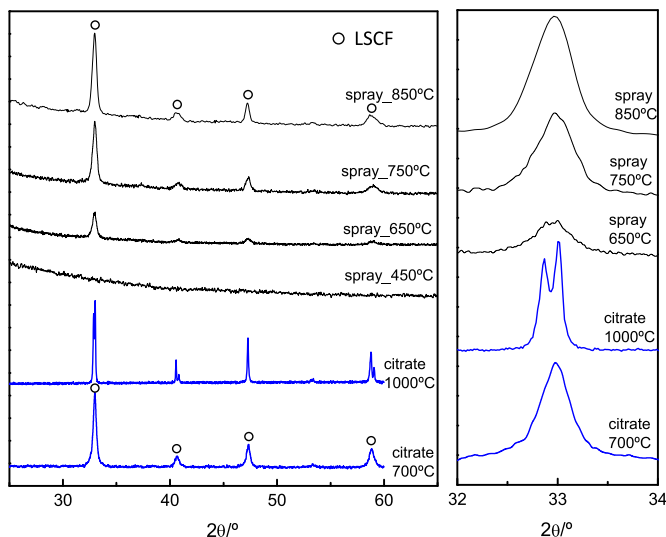

Fig. 1. XRD patterns of LSCF powders obtained by citrate precursor method at 700 and 1000 °C and LSCF film deposited on quartz substrates by spray-pyrolysis at 450 °C and after thermal treatment between 650 and 850 °C for 5 h.
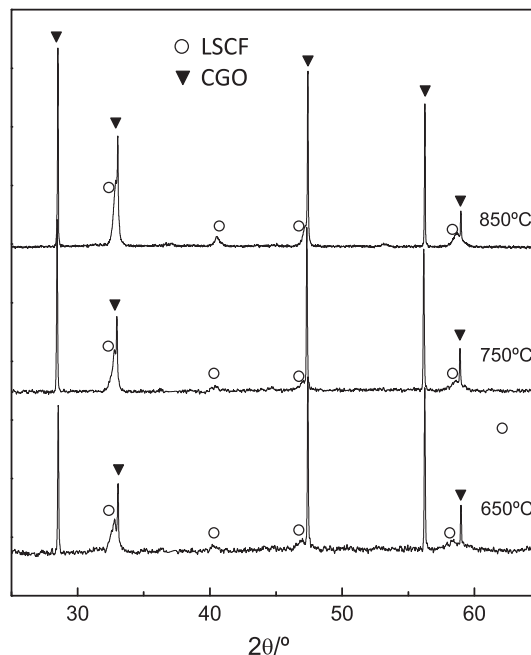

Fig. 2. XRD patters of LSCF films deposited on CGO pellets at 450 °C and calcined between 650 and 850 °C for 5 h.
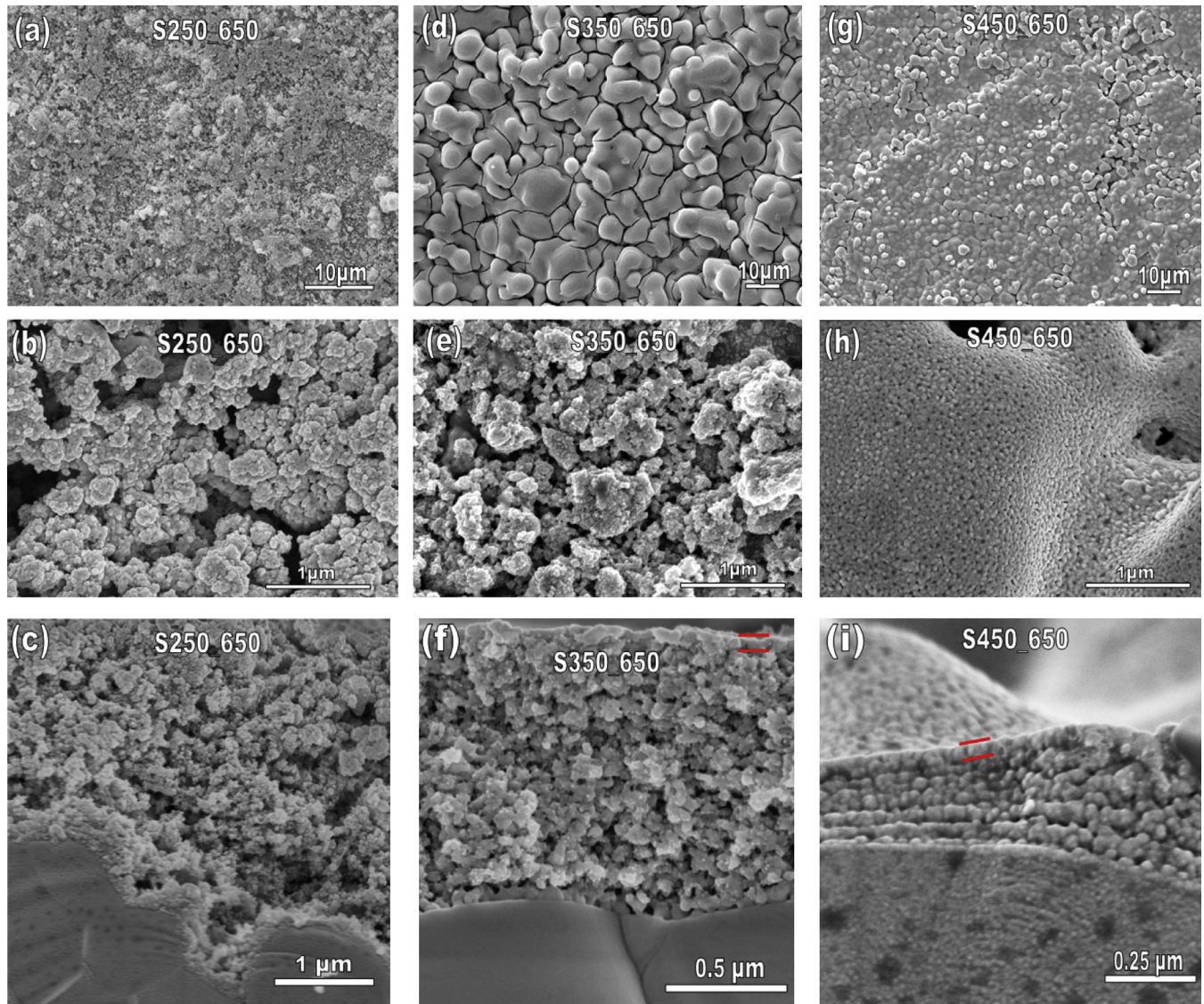
Fig. 3. SEM of the surface morphology and cross-section of LSCF cathodes deposited by spray-pyrolysis on CGO pellets at (a–c) 250 °C, (d–f) 350 °C and (g–i) 450 °C after calcination at 650 °C for 5 h.

The superficial morphology of LSCF films, annealed at 650 and 850 °C for 5 h, is shown comparatively in Fig. 4. For all the films is observed that the superficial porosity decreases with the increasing of annealing temperature. The grain size distribution is shown in the insets of Fig. 4 and the average grain sizes are listed in Table 1. The average grain size for the films annealed at 650 °C decreases with the increasing of deposition temperature from 55 nm at 250 °C to 30 nm at 450 °C. LSCF cathode deposited at 450 °C shows a macroporous microstructure with pore size lower than 50 nm and much finer grain size 30 nm compared to the film deposited at 250 °C–55 nm (Fig. 4c). As expected, the grain size grows after annealing at 850 °C, while the superficial porosity decreases (Fig. 4d–f). The grain size for S250 sample increases slightly with the temperature from 55 nm at 650 °C to 60 nm at 850 °C and large variation occurs for S450, 30–78 nm (Table 1). This behaviour can be explained by the different porosity of the films, indeed, it is known from the literature that occurrence of the pores strongly affects the grain growth kinetics [21,33]. It should be also commented that the grain size is somewhat larger than those estimated by XRD, suggesting that grains are formed by several diffraction domains (Table 1).

3.3. Electrical characterization

The impedance spectra for S250, S350 and S450 symmetrical cells, under open circuit voltage (OCV) and at various measured temperatures in air, are shown in Fig. 5. The electrolyte resistance was subtracted for easier comparison of the electrode response. Depending on the temperature range different contributions are observable in the spectra. At temperatures higher than 550 °C only the arcs attributed to the electrode processes are observed (Fig. 5a, d and g). Between 350 and 500 °C the arc ascribed to grain boundary conduction (GB) in the electrolyte is also visible (Fig. 5b, e and h). Finally, the grain interior (bulk) contribution of the electrolyte appears below 350 °C at high frequencies (Fig. 5c, f and i).

Different equivalent circuits were tested to fit the data, however the best results were obtained using the model based on (RQ) elements in series, each one being assigned to a specific electrochemical phenomenon, where R is a resistance in parallel with a constant phase element Q with impedance: $Z_Q = (jwQ)^{-n}$ to take into consideration the depressed arcs. The equivalent circuits used for fitting the spectra are shown in the inset of Fig. 5d–f. In the high
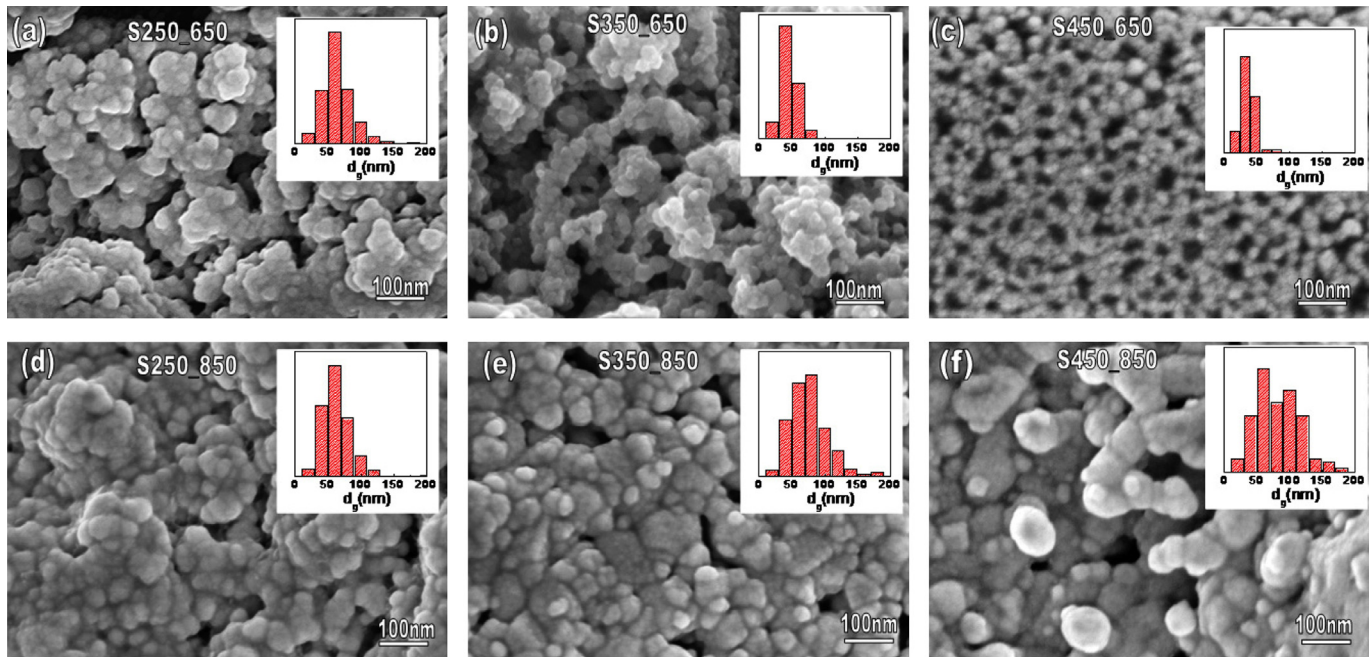
Fig. 4. SEM image of surface morphology at higher magnification for LSCF cathodes deposited on CGO pellets at 250, 350 and 450 °C and post-thermal treatment at 650 °C and 850 °C for 5 h. The insets show the grain size distribution.

and intermediate temperature ranges a serial inductance: $Z_L = jwL$ was included to simulate the inductive effects of the setup at high frequencies, which was found to take a value of around 10^{-6} H. A serial R_s and/or (RQ) elements were used to simulate the grain interior (GI) and grain boundary (GB) contributions of the CGO electrolyte (inset of Fig. 5d and e).

The electrode response of LSCF is typically composed of two or three contributions depending on the electrode composition, microstructure and measured temperature [34–39]. In the present study, the electrode contribution show similar shape for all the cells and the experimental data were adequately simulated by using two serial (RQ) elements between 350 and 650 °C in air atmosphere. These two contributions are usually attributed to surface chemical exchange of O_2 and solid state oxygen diffusion [3].

The following parameters were obtained for each contribution: the resistance R_i, the pseudocapacitance Q_i and the exponential parameter n_i of the bulk, grain boundary and electrode processes. These parameters are related to the angular relaxation frequency w_i and true capacitance C_i by the following relation:

$$w_i = \frac{1}{R_i C_i} = \frac{1}{(R_i Q_i)^{1/n_i}} \tag{1}$$

The bulk and grain boundary contributions show typical capacitance values of $\sim$pF cm^{-1} and $\sim$nF cm^{-1}, respectively, whereas the capacitance of the electrode processes is $\sim$mF cm^{-2}.

The total resistance of the electrolyte did not vary with the deposition temperature and the post-annealing treatment of the LSCF film, suggesting negligible reaction between LSCF and CGO in the operating temperature range. However, the electrode resistance increased significantly with the annealing treatment, especially for those films deposited at high temperatures >350 °C, as a consequence of the microstructural changes of the electrodes and the reduced reaction sites for ORR (Fig. 5g–i).

3.3.1. Contributions of the electrode polarization in air

The contributions of the electrode response at high frequency (HF) and medium frequency (MF) were studied separately as a function of the deposition and post-deposition temperature of the films.

Fig. 6a displays the variation of relaxation frequency for a representative sample S350. For all samples the relaxation frequency associated at each contribution decreases with the annealing temperature, whereas the capacitance increases slightly (Fig. 6b). The relaxation frequencies were in the range of 0.1–10^3 Hz and 1–10^4 Hz for the MF and HF contributions, respectively, in the temperature range 300–650 °C, following an Arrhenius type dependence on the temperature. The capacitance of the HF contribution increases with the annealing temperature from 0.5 to 1.2 mF cm^{-2} and they are nearly independent on the measured temperature consistent with an interfacial capacitance coupled with charge transfer process. These values are similar to those previously reported on dense and porous LSCF films, which was attributed to the interfacial LSCF/CGO charge transfer [19,36,38]. The assignment of HF response to ionic transfer process at the electrolyte/electrode interface is further corroborated in the next

Table 1
Deposition conditions, microstructural features of the LSCF films (d_g: average grain size and t: thickness). Activation energies for the high (HF) and medium frequency (MF) contributions to the polarization in air atmosphere and the area specific resistance (ASR).

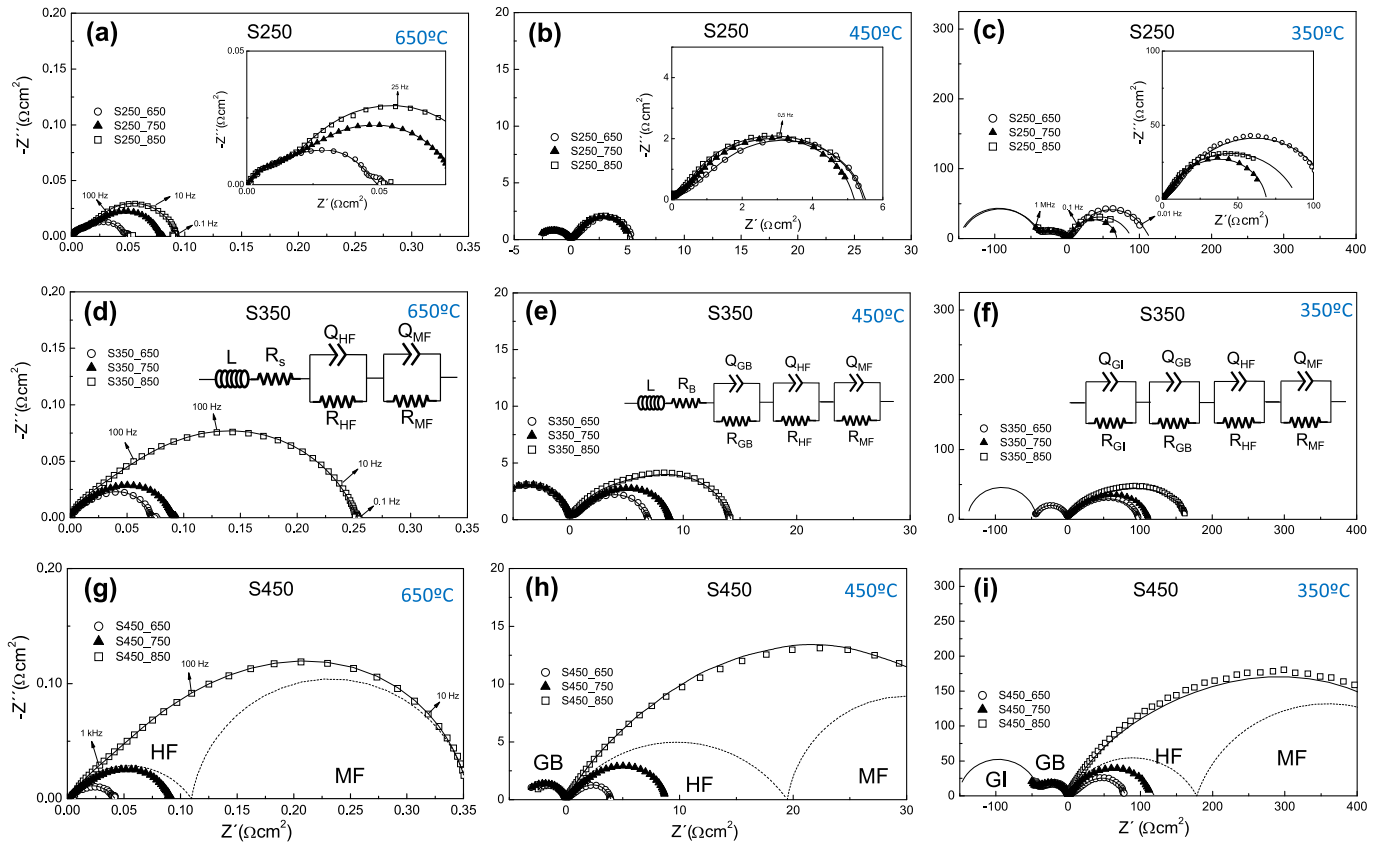| Sample	Deposition T (°C)	Annealing T (°C)	d_g (nm)	t (μm)	E_{HF} (eV)	E_{MF} (eV)	E_{ASR} (eV)
S250_650	250	650	55	3	1.18	1.29	1.22
S250_750		750	–		1.12	1.20	1.15
S250_850		850	61		1.19	1.23	1.15
S350_650	350	650	45	1.25	1.14	1.24	1.17
S350_750		750	–		1.17	1.30	1.11
S350_850		850	71		1.05	1.10	1.06
S450_650	450	650	30	0.25	1.20	1.27	1.24
S450_750		750	–		1.30	1.29	1.21
S450_850		850	78		1.44	1.38	1.17

Fig. 5. Impedance spectra of LSCF cathodes deposited symmetrically on CGO electrolyte pellets at (a–c) 250 °C, (d–f) 350 °C and (g–i) 450 °C and post-thermal treatment at 650, 750 and 850 °C for 4 h. The impedance spectra are shown at different measurement temperatures (a, d, g) 650 °C, (b, e, h) 450 °C and (c, f, i) 350 °C. The insets of (d–f) show the equivalent circuits used to fit the spectra in the different temperature ranges. The line plots correspond to the fitting result obtained with equivalent circuits.

section by evaluating the dependence of R_{HF} versus pO_2. The MF contribution with a capacitance of 5–10 mF cm^{-2} is possibly attributed to oxygen ionic bulk diffusion as already suggested by LSCF based cathodes [19,36,38].

The Arrhenius representation of the HF and MF resistances for S250 and S450 samples annealed at different temperatures are shown in Fig. 7. The MF response is the largest contribution to the total polarization for all the samples and especially at low
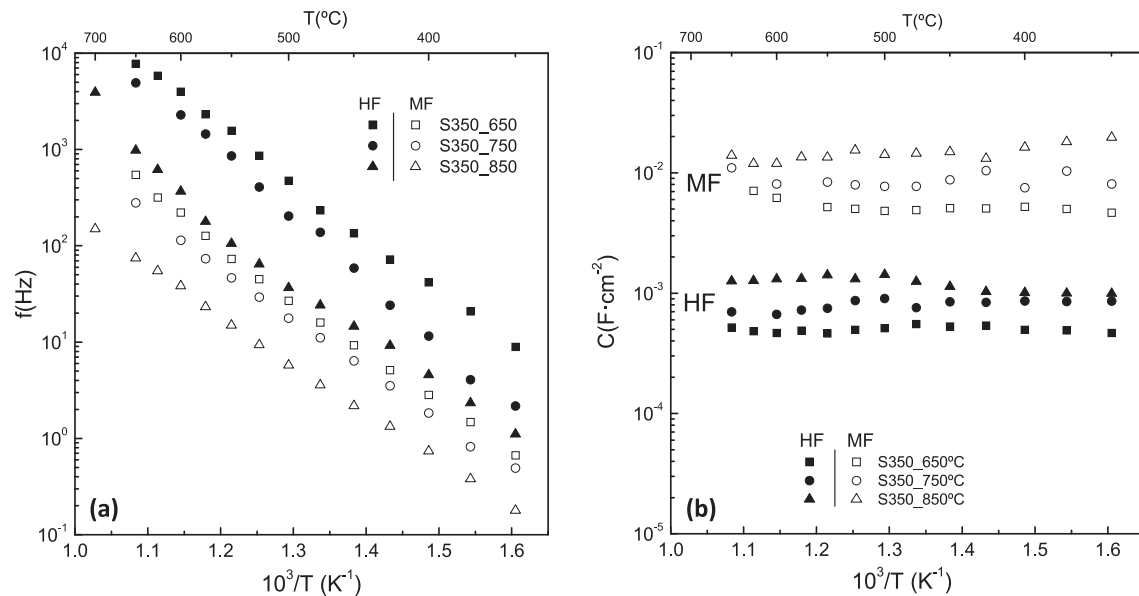

Fig. 6. (a) Relaxation frequencies and (b) capacitances of the high (HF) and medium frequency (MF) contributions for S350 sample after post-treatment at 650, 750 and 850 °C versus the reciprocal temperature.
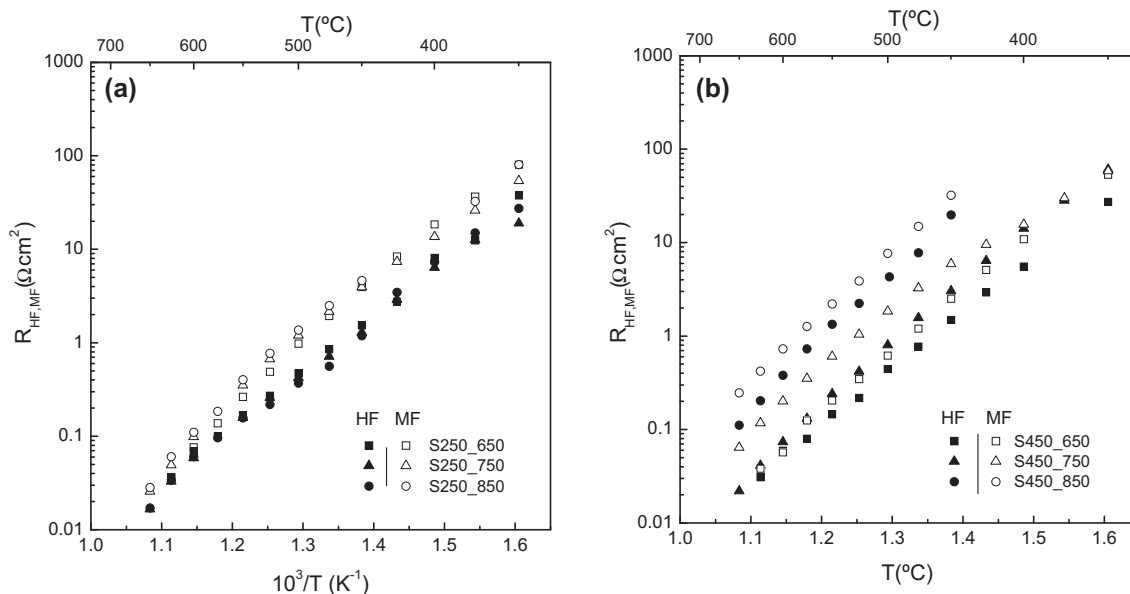
Fig. 7. Arrhenius plots of the high (HF) and medium frequency (MF) contributions to the polarization resistance for (a) S250 and (b) S450 samples after post-annealing between 650 and 850 °C for 5 h.

temperatures. In the case of S250 sample the values of R_{HF} and R_{MF} change little with the annealing temperature (Fig. 7a), in contrast, both resistances increase for S450 sample (Fig. 7b). The corresponding activation energies for R_{HF} and R_{MF} contributions are similar 1.1–1.3 eV for the different samples annealed at 650 °C, although it seems to increase with the deposition temperature with a maximum value of 1.4 eV determined for S450_850 (Table 1).

It should also be commented that above 700 °C a new contribution begins to appear in the spectra at low frequency, with a large capacitance value of ~ 1 F cm^{-2}, and this become more important as the temperature increases (Fig. S1, Supplementary content). Moreover, this process was also observed at low oxygen partial pressures, showing a strong dependence on pO_2 and therefore is possibly attributed to gas-phase diffusion limitations. This behaviour is not surprising because gas-phase diffusion becomes more important at high temperatures compared to the other electrode contributions due to its low activation energy [3].

3.3.2. pO₂ dependence of the polarization resistance

In order to obtain further insights on the different rate-limiting-steps of the electrode polarization, the resistance dependency associated at each response was studied at different temperatures as a function of pO_2. The measurements were carried out between 1 and 0.01 atm of pO_2 to neglect the influence of the oxygen stoichiometry of the compounds on the electrode performance. It is well reported that the loss of lattice oxygen in LSCF depends on the cathode composition, oxygen partial pressure and temperature, affecting greatly the electrode performance [40].

The impedance spectra of S250_850 sample at 650 °C and different pO_2 values are shown in Fig. 8. At $pO_2 > 0.1$ atm two processes are discernible at high and intermediate frequencies with relaxation frequency of $f_{HF} = 2$–10 kHz and $f_{MF} = 10$–600 Hz respectively. At lower oxygen partial pressures a third contribution, with relaxation frequency of $f_{LF} = 0.2$–10 Hz, begins to appear, which becomes dominant at reducing pO_2 (inset Fig. 8). In this case three (RQ) elements were used to fit the data. A similar behaviour was observed by Escudero et al. for La₂NiO₄ cathode, where a new arc was detected at $pO_2 < 0.1$ atm [41].

The different steps of oxygen reduction are dependent on the oxygen partial pressure, and the relationship between the resistance of each contribution and the pO_2 can be expressed as [42–44]:

$$R_i = k(pO_2)^{-m} \tag{2}$$

where k is a constant and m an exponent that depends on the kinetic limiting step. If $m = 1$ the limiting process is oxygen diffusion in the gas phase or molecular adsorption on the surface of the electrode, $m = 1/4$ charge transfer and $m = 1/2$ oxygen dissociation.

Fig. 9 shows the resistance variation of the different contributions with the pO_2 for S250_850 sample at different measured temperatures.
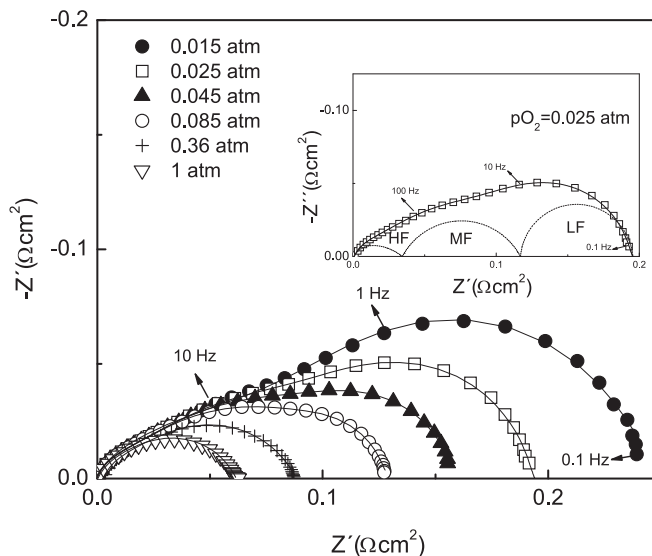

Fig. 8. Impedance spectra for S250_850 sample as a function of the oxygen partial pressure at a measured temperature of 650 °C.
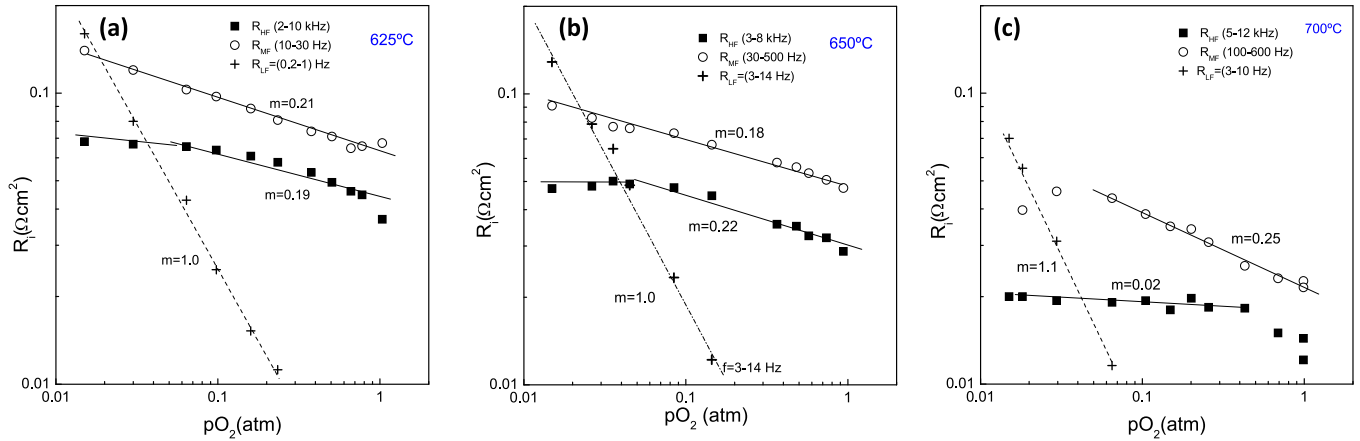
Fig. 9. Contributions of the electrode resistance for S250_850 sample as a function of the oxygen partial pressure at different temperatures: (a) 625, (b) 650 and (c) 700 °C.

The HF process has a capacitance values of $C_{HF} = 0.2$–0.4 mF cm^{-2} and a change of m is observed from $m = 0.16$–0.19 at high pO_2 to $m \sim 0$ at low pO_2 (Fig. 9). Marhina et al. studied the polarization resistance of La$_{0.6}$Sr$_{0.2}$Co$_{0.2}$Fe$_{0.8}$O$_{3-\delta}$ films between 1 and 10^{-4} atm and also found a weak dependence of R_{HF} versus pO_2 with m values of 0.06–0.1 in the high temperature range [38]. This contribution was assigned to the ionic conduction at the LSCF/CGO interface.

The medium frequency contribution is the most important limiting step of the polarization resistance at $pO_2 > 0.01$ atm and has capacitance of $C_{MF} = 3$–10 mF cm^{-2}. Moreover, R_{MF} shows a weak pO_2 dependence with m values between 0.18 and 0.28 and therefore is possibly attributed to ionic bulk diffusion in agreement to previous results [38,39].

The low frequency process (observed at low pO_2) has a strong dependence on pO_2 $m = 1$. Moreover, it exhibits a large capacitance $C_{LF} = 0.1$–0.4 F cm^{-2} and therefore is related to gas-phase diffusion at high temperature. Similarly, Adler et al. reported that at $pO_2 < 0.01$ atm the electrode kinetics of porous La$_{1-x}$Sr$_x$CoO$_{3-\delta}$ cathodes become dominated by gas-phase diffusion [45].

The behaviour of the total polarization resistance versus pO_2 shows a linear relationship in pO_2 range (1–0.01 atm) with m

values of 0.25, 0.27 and 0.29 at 625, 650 and 700 °C, respectively (Fig. S2, Supplementary content). At $pO_2 < 0.01$ atm an increase of m is expected due to the dominating LF contribution in this region (gas-phases diffusion with $m = 1$). Therefore, these results are similar to those found previously for thin films and thick LSCF cathodes with $m = 0.2$ at $pO_2 > 10^{-2}$ atm and $m = 0.7$ at $pO_2 < 10^{-2}$ atm at a measured temperature of 600 °C [35,38].

3.3.3. Area specific resistances

The area specific resistance (ASR) under open circuit voltage was calculated from the addition of the each polarization contribution R_i, as follows:

$$\text{ASR} = \frac{R_{\text{pol}} \cdot S}{2} \qquad (3)$$

where S is the effective electrode area and R_{pol} the total polarization resistance, which was divided by two due to the symmetrical configuration of the cells.

The Arrhenius plots of ASR are shown in Fig. 10. A nearly linear dependence is observed for the different samples treated between
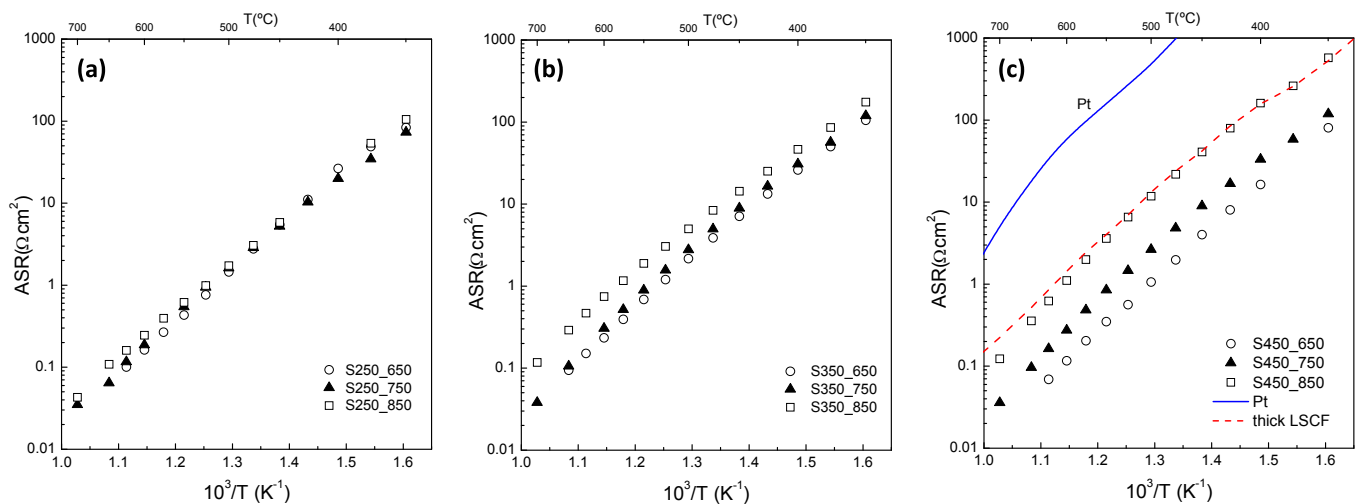

Fig. 10. Arrhenius plots of the overall polarization resistance for LSCF cathodes deposited symmetrically by spray-pyrolysis on CGO pellets at (a) 250 °C, (b) 350 °C and (c) 450 °C for 1 h and after thermal treatment at 650, 750 and 850 °C for 5 h. The polarization resistance obtained with a thick LSCF cathode and with only Pt electrodes are also included for comparison purpose in (c).

650 and 850 °C. One can observe that major differences with the annealing temperature occur for S450 sample (Fig. 10c).

At an annealing temperature of 650 °C the values of ASR are very similar for the different electrodes, despite the different electrode thickness 0.25–3 μm, taking minimum and maximum values of 0.04 and 0.06 Ω cm^2 for S300_650 and S450_650, respectively, at a measured temperature of 650 °C (Fig. 11). Note that ASR values are expected to decrease with increasing electrode thickness because of the increased reaction sites for oxygen reduction, however, beyond a certain thickness the benefits of the increase of the active layer are counterbalanced by the increasing migration length for ion, rendering constant values of ASR. Hence, the similar performance for all electrodes annealed at 650 °C is apparently due to the lower particle size and large surface area of the films deposited at higher temperature (Table 1). This means that the most important electrochemical reactions in these films occur close to the electrolyte interface <1 μm as previously suggested for LSCF thin films [19]. In addition, considering that the film thickness of S450 sample is relatively small ∼0.25 μm, one may expect a further decrease of the ASR values by increasing the deposition time.

After the subsequent post-annealing treatment at 750 and 850 °C the grain size grows and the porosity decreases, and as a consequence the number of actives sites for ORR are reduced, resulting in an increase of ASR. This effect is more pronounced in the case of the macroporous films deposited at 450 °C (Fig. 10c). However, the films deposited at lower temperature, S250, exhibit lower microstructural changes with the sintering temperature and high performance is obtained even after annealing at 850 °C for 5 h (Figs. 10a and 11). The samples annealed at 850 °C have ASR values of 0.1 and 0.6 Ω cm^2 for S250_850 and S450_850 respectively (measured at 650 °C). It is worth nothing that these values are comparable to those obtained for a thick LSCF cathode (∼40 μm of thickness) deposited by screen-printing at a sintering temperature of 900 °C–0.52 Ω cm^2 (Figs. 10c and 11).

Thus the ASR values are clearly related to the electrode-pore surface area of the films. For this reason, macroporous and porous LSCF films obtained at 450 and 250 °C, respectively, exhibit a similar performance if the annealing temperature is lower than 750 °C. However, when the annealing temperature increases above 750 °C the macroporous microstructure of S450 collapses and the performance decreases drastically, whereas samples with initial high porosity, S250, retain the porous microstructure and smaller degradation of the performance is observed.

The values of activation energy ranged between 1.1 and 1.2 eV (Table 1), suggesting that the reaction mechanism in LSCF films is not affected by the deposition and annealing temperature. Similar values were reported previously for LSCF thin films (1.0–1.2 eV) [34–38].

Another important issue to be considered is the stability of the films with the annealing time. The stability of S250 sample was evaluated for 2 days at 650 °C and both the serial and polarization resistance showed a degradation of about 5%, which is related to microstructural changes of the electrodes and possible reaction or interdiffusion at the electrolyte–electrode interface. Further studies are in progress to evaluate the stability of these materials after long term operation.

4. Conclusions

La$_{0.6}$Sr$_{0.4}$Co$_{0.8}$Fe$_{0.2}$O$_{3-\delta}$ (LSCF) thin film cathodes have been deposited on quartz substrates and on CGO pellets by conventional spray pyrolysis using an aqueous solution of metal nitrates. The deposition temperature was the only variable parameter in the different depositions, which varied between 250 and 450 °C. By depending on the deposition temperature different electrode morphologies were obtained: highly porous at 250 °C, cracked and porous at 350 °C and macroporous at 450 °C. The grain size increased from 30 to 80 nm with the annealing temperature 650–850 °C.

Electrochemical measurements were performed by impedance spectroscopy on symmetrical cells in air and as a function of the oxygen partial pressure to identify the different limiting steps of the electrode polarization. Three contributions were observed depending on the temperature and the oxygen partial pressure. The high and intermediate frequency contributions were identified as ionic transfer at the electrolyte/electrode interface and ionic diffusion in the LSCF bulk, respectively. The low frequency contribution is only visible at high temperatures >700 °C and/or low oxygen partial pressure and showed a strong dependence on pO_2 and was attributed to gas-phase diffusion of oxygen. All cells annealed at 650 °C showed low ASR values of 0.04–0.06 Ω cm^2 measured at 650 °C. Higher annealing temperatures result in a decrease of the electrode-pore surface area and consequently the ASR increased. However, LSCF electrodes deposited at 250 °C, with high porosity, exhibited lower microstructural changes with the heat treatment and ASR values of 0.05 and 0.1 Ω cm^2 were obtained after annealing at 650 and 850 °C respectively.

Appendix A. Supplementary data

Supplementary data related to this article can be found at http://dx.doi.org/10.1016/j.jpowsour.2014.01.021.
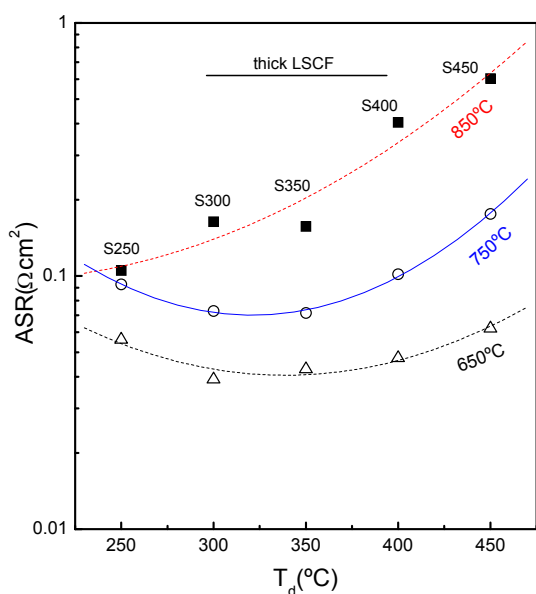

Fig. 11. Overall polarization resistance at 650 °C for LSCF cathodes in air as a function of the deposition temperature T_d and the post-thermal treatment at 650, 750 and 850 °C for 5 h.

References

[1] N.Q. Minh, T. Takahashi, Science and Technology of Ceramic Fuel Cell, Elsevier, N.Y., 1995.

[2] B.C.H. Steele, A. Heinzel, Nature 414 (2001) 345−352.
[3] S.B. Adler, Chem. Soc. Rev. 104 (2004) 4791−4843.
[4] J. Fleig, Annu. Rev. Mater. Res. 33 (2003) 361−382.
[5] E.V. Tsipis, V.V. Kharton, J. Solid State Electrochem. 12 (2008) 1039−1060.
[6] L.-W. Tai, N.M. Nasrallah, H.U. Anderson, D.M. Sparlin, S.R. Sehlin, Solid State Ionics 76 (1995) 259−271.
[7] Z. Shao, S.M. Haile, Nature 431 (2004) 170−173.
[8] A. Tarancón, S.J. Skinner, R.J. Chater, F. Hernández-Ramírez, J.A. Kilner, J. Mater. Chem. 17 (2007) 3175−3181.
[9] S. Švarcová, K. Wiik, J. Tolchard, H.J.M. Bouwmeester, T. Grande, Solid State Ionics 178 (2008) 1787−1791.
[10] A.S. Joshi, K.N. Grew, A.A. Peracchio, W.K.S. Chiu, J. Power Sources 164 (2007) 631−638.
[11] D. Marrero-López, J.C. Ruiz-Morales, J. Peña-Martínez, J. Canales-Vázquez, P. Núñez, J. Solid State Chem. 181 (2008) 685−692.
[12] J.C. Ruiz-Morales, D. Marrero-López, M. Gálvez-Sánchez, J. Canales-Vázquez, C. Savaniu, S.N. Savvin, Energy Environ. Sci. 3 (2010) 1670−1681.
[13] D. Beckel, A. Bieberle-Hütter, A. Harvey, A. Infortuna, U.P. Muecke, M. Prestat, J.L.M. Rupp, L.J. Gauckler, J. Power Sources 173 (2007) 325−345.
[14] A. Princivalle, D. Perednis, R. Neagu, E. Djurado, Chem. Mater. 16 (2004) 3733−3739.
[15] A. Princivalle, D. Perednis, R. Neagu, E. Djurado, Chem. Mater. 17 (2005) 1220−1227.
[16] C.-L. Chang, C.-S. Hsu, B.-H. Hwang, J. Power Sources 179 (2008) 734−738.
[17] C.-L. Chang, T.F. Chu, C.S. Hsu, B.H. Hwang, J. Eur. Ceram. Soc. 32 (2012) 915−923.
[18] L. Dieterle, P. Bockstaller, D. Gerthsen, J. Hayd, E. Ivers-Tiffée, U. Guntow, Adv. Energy Mater. 1 (2011) 249−258.
[19] D. Marinha, L. Dessemond, J.S. Cronin, J.R. Wilson, S.A. Barnett, E. Djurado, Chem. Mater. 23 (2011) 5340−5348.
[20] D. Beckel, U.P. Muecke, T. Gyger, G. Florey, A. Infortuna, L.J. Gauckler, Solid State Ionics 178 (2007) 407−415.
[21] N.I. Karageorgakis, A. Heel, A. Bieberle-Hütter, J.L.M. Rupp, T. Graule, L.J. Gauckler, J. Power Sources 195 (2010) 8152−8161.
[22] I. Taniguchi, R.C. van Landschoot, J. Schoonman, Solid State Ionics 156 (2003) 1−13.
[23] C.-S. Hsu, B.-H. Hwang, J. Electrochem. Soc. 153 (2006) A1478−A1483.
[24] R. Ayouchi, F. Martin, J.R. Ramos Barrado, M. Martos, J. Morales, L. Sanchez, J. Power Sources 87 (2000) 106−111.
[25] D. Marrero-López, J. Peña-Martínez, J.C. Ruiz-Morales, D. Pérez-Coll, M.C. Martín-Sedeño, P. Núñez, Solid State Ionics 178 (2007) 1366−1378.
[26] J. Rodríguez-Carvajal, Phys. B: Condens. Matter 192 (1993) 55−69.
[27] X'Pert HighScore Plus, Version 2.0a, PANalytical BV, 2004.
[28] J.C.C. Abrantes, Estereologia, Software Package, ESTG/IPVC, Portugal, 2001.
[29] D. Johnson, ZView: A Software Program for IES Analysis, Version 2.9, Scribner Associates, Inc., Southern Pines, NC, 2005.
[30] S. Wang, M. Katsuki, M. Dokiya, T. Hashimoto, Solid State Ionics 159 (2003) 71−78.
[31] V.G. Sathe, S.K. Paranjpe, V. Siruguri, A.V. Pimpale, J. Phys. Condens. Matter 10 (1998) 4045−4055.
[32] L.M. Acuña, J. Peña-Martínez, D. Marrero-López, R.O. Fuentes, P. Núñez, D.G. Lamas, J. Power Sources 196 (2011) 9276−9283.
[33] W.D. Kingery, B. Francois, J. Am. Ceram. Soc. 48 (1965) 546−547.
[34] N.J. Simrick, A. Bieberle-Hütter, T.M. Ryll, J.A. Kilner, A. Atkinson, J.L.M. Rupp, Solid State Ionics 206 (2012) 7−16.
[35] N. Grunbaum, L. Dessemond, J. Fouletier, F. Prado, L. Mogni, A. Caneiro, Solid State Ionics 180 (2009) 1448−1452.
[36] F.S. Baumann, J. Fleig, H.-U. Habermeier, J. Maier, Solid State Ionics 177 (2006) 1071−1081.
[37] A. Ringuedé, J. Fouletier, Solid State Ionics 139 (2001) 167−177.
[38] D. Marinha, L. Dessemond, E. Djurado, J. Power Sources 197 (2012) 80−87.
[39] M. Shah, S.A. Barnett, Solid State Ionics 179 (2008) 2059−2064.
[40] D. Mantzavinos, A. Hartley, I.S. Metcalfe, M. Sahibzada, Solid State Ionics 134 (2000) 103−109.
[41] M.J. Escudero, A. Aguadero, J.A. Alonso, L. Daza, J. Electroanal. Chem. 611 (2007) 107−116.
[42] E. Siebert, A. Hammouche, M. Kleitz, Electrochim. Acta 11 (1995) 1741−1753.
[43] Z. Jiang, Z. Lei, B. Ding, C. Xia, F. Zhao, F. Chen, Int. J. Hydrogen Energy 35 (2010) 8322−8330.
[44] Grimaud, F. Mauvy, J. Marc Bassat, S. Fourcade, M. Marrony, J. Claude Grenier, J. Mater. Chem. 22 (2012) 16017−16025.
[45] S.B. Adler, Solid State Ionics 111 (1998) 125−134.